paper by Smith [N. V. Smith, Phys. Rev. B 3, 1862 (1971)] appeared giving the energy difference $E(X_5) - E(X_1)$ of 3.88 eV, obtained from a very detailed analysis of his photoemission data.

[18]E. C. Snow, Phys. Rev. 172, 708 (1968).

[19]N. E. Christensen, Phys. Status Solidi 31, 635 (1969).

[20]S. Bhatnagar, Phys. Rev. 183, 657 (1969).

[21]P. E. Lewis and P. M. Lee, Phys. Rev. 175, 795 (1968).

[22]R. L. Jacobs, J. Phys. C 1, 1296 (1968); 1, 1307 (1968).

[23]V. Heine and I. Abarenkov, Phil. Mag. 9, 451 (1964); I. Abarenkov and V. Heine, *ibid.* 12, 529 (1965); A. O. E. Animalu and V. Heine, *ibid.* 12, 1249 (1965).

[24]M. J. G. Lee, Phys. Rev. 187, 901 (1969).

[25]J. F. Cooke, H. L. Davis, and R. F. Wood, Phys. Rev. Letters 25, 28 (1970).

PHYSICAL REVIEW B VOLUME 4, NUMBER 6 15 SEPTEMBER 1971

Radio-Frequency Size Effect in Magnesium†

Paul Roach
Department of Physics, University of Chicago, Chicago, Illinois 60637
(Received 2 November 1970)

The radio-frequency size effect has been used to study the Fermi surface of magnesium. These experimental data are then compared with a detailed mathematical model of the Fermi surface. The agreement is very good, confirming the accuracy of the experimental technique and the mathematical model. However, certain problems of data interpretation seriously limit the applications of the radio-frequency size effect for the study of unknown Fermi surfaces. Experiments for which this technique is better suited are discussed.

I. INTRODUCTION

The radio-frequency size effect (RFSE) is a relatively recent technique for the study of the Fermi surfaces of metals. Since the initial experiments on tin by Gantmakher,[1] this technique has been applied to an ever increasing variety of metals. The primary attraction of this method is its ability to give accurate measurements of Fermi-surface caliper dimensions. When combined with the relatively simple experimental apparatus that is required, the RFSE offers a powerful and convenient tool for the study of metallic Fermi surfaces.

Full references to the early work with the RFSE are contained in the review articles by Gantmakher[2] and by Walsh.[3] Most of this work falls into two categories: the study of known simple Fermi surfaces in order to obtain a better understanding of the RFSE itself, and the study of unknown complex Fermi surfaces in order to learn about the band structure of the particular metal. Both of these approaches fail to define the limitations to the use of the RFSE: the former, because a simple surface, as in potassium,[4] does not present the problems of interpretation that can arise with a complex surface; the latter, because an unknown surface, as in gallium,[5] provides little or no basis for resolving problems of interpretation.

One of the purposes of this paper is to define more clearly some of the limitations in the usefulness of the RFSE. The results of this study make it possible to suggest areas where the RFSE can be used to great advantage. But to do this, it is essential to use a metal whose Fermi surface is both topologically complex and well known.

Magnesium is well suited to these goals. On the one hand, it has a geometrically complex Fermi surface which can be expected to cause a variety of complicated effects in the experimental data. It is just such effects that are important for this study since their interpretation is one of the major problems in the use of the RFSE.

On the other hand, the Fermi surface has been accurately measured and described in terms of a detailed band-structure model by Stark *et al.*[6–8] Calculations based on this mathematical model can be compared directly with the experimental data, even for the most complicated signals. In this way, the accuracy and reliability of the experimental method can be clearly defined.

II. SIZE EFFECT

From a purely experimental viewpoint, the RFSE measures the rf power absorption in a metal sample as a function of static magnetic field strength. The problem then is to relate this power absorption to the motion of the electrons in the sample. As is implied by the name "size effect," this motion is expected to be strongly influenced by the presence of the sample boundaries as well as by the static magnetic field and the Fermi-surface geometry.

The purpose of the rf field is to interact with the electrons in the metal and thereby probe their motion. But since the rf field penetrates only a

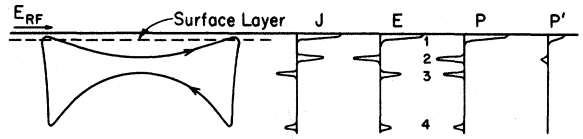

FIG. 1. Cross section of sample showing typical trajectory.

small distance into the sample (the skin depth), this interaction must necessarily occur at the surface. It is this feature of the experiment that gives the RFSE its high selectivity for certain types of electron trajectories in the metal.

In order for an electron on some trajectory to interact effectively with the external rf field, it must enter the skin layer and also spend a significant amount of time there. This requires that the electron velocity be essentially parallel to the surface when it enters the skin layer. In general, any trajectory that has a turning point (velocity parallel to the surface) in the skin layer will interact effectively with the rf field.

In Fig. 1, a cross section of the sample is shown, together with a typical electron trajectory. (The static magnetic field is normal to the drawing.) The trajectory shown has six turning points, with two in the skin layer. As a result of the interaction at the surface, the electron receives a small increment of velocity parallel to the surface which is then carried along the trajectory into the bulk of the sample. This excitation will reappear at those depths in the sample where the electron is again moving parallel to the surface. At these depths there will appear distinct spikes in the current density J and the electric field E which are images of the current and field at the surface. Figure 1 also shows these current and field spikes as well as the power absorption P. The peaks numbered 2—4 occur at depths corresponding to turning points on the trajectory in the bulk of the sample.

As the static magnetic field varies, the dimensions of all of the trajectories and their associated current and field distributions will expand and contract as B^{-1}. One side of each effective trajectory is fixed at the surface by the requirement that one turning point be within the skin layer; but the penetration of the trajectory into the bulk varies with the magnetic field. The presence of the second surface of the sample will then allow the current and field distributions to be analyzed.

In effect, the interaction at one surface provides the excitation while the interaction at the second surface detects it. But there are two distinct types of interaction at the second surface. In the dominant mode, the electron trajectory intersects the second surface and the electron is scattered out of its effective trajectory. Before the onset of this type of interaction (i. e., at magnetic fields sufficiently large that the trajectory is completely contained in the sample), the electron will complete many revolutions around the trajectory. This is assured by satisfying the experimental condition $\Omega\tau \gg 1$, where Ω is the cyclotron frequency and τ is the bulk scattering lifetime. At each revolution, the electron absorbs rf energy at the surface and then makes an additional contribution to the fields and currents in the interior of the sample. These contributions add in the same phase for each revolution because the frequency of the applied rf field is kept so low that the rf field strength is effectively constant during the scattering lifetime of an electron.

But at lower magnetic fields, the trajectory will intersect the second surface and the electron will be scattered after only one revolution. This is in contrast with the $\Omega\tau$ effective revolutions that occurred at higher magnetic fields. Therefore, the power absorption associated with this trajectory (as well as the internal currents and fields) must decrease by a factor $\Omega\tau$. This change in the power absorption is then detected by the experimental apparatus.

The critical value of magnetic field that marks the transition from one stage to the other is the value B_c at which the diameter of the trajectory is just equal to the sample thickness. At this value of field, the electron interacts effectively with the rf field at one surface and begins to be scattered at the opposite surface. It is here that one expects to see a change in the power absorption. And since the trajectory dimension D need only change by δ, the skin depth, for the transition to be complete, this change will be quite abrupt, occurring within a field range ΔB. If $D > d$ (d is the sample thickness), all trajectories intersect the surface, and if $D < d - \delta$, none of the effective trajectories will intersect the surface. Thus, we have $\Delta B/B_c \cong \delta/d$.

The other way in which the trajectories can interact with the second surface is by coupling to the external rf field that is present there. Each of the turning points on the trajectory is associated with a spike in the currents and fields in the sample (see Fig. 1), and these can interact with the external rf field whenever they enter the skin layer. Such interactions will cause changes in the power absorption in the sample and may be considered independent of the first effect, trajectory cutoff.

As the trajectory expands under the influence of a decreasing magnetic field, such as interaction first occurs when the diameter of the trajectory (in the sense of a caliper dimension) just spans the sample. This is simultaneous with the trajectory cutoff already described.

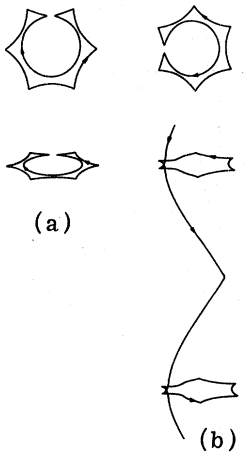

FIG. 2. Comparison of (a) $\vec{k}$-space orbit and (b) real-space trajectory.

After trajectory cutoff, the internal currents and fields are much smaller, as shown schematically in the plot of power P' in Fig. 1. Nevertheless, it is frequently possible to detect such field spikes as they enter the skin layer at the second surface. In this way, the experiment can provide more information about a trajectory than just its over-all caliper dimension (the maximum distance between turning points, measured in the direction normal to the surface). The entire field and current distribution associated with the trajectory is analyzed by the interaction at the second surface. This, in principle, gives the location of all of the turning points on the trajectory.

The importance of this type of experiment lies in the relationship between the real-space trajectories and the Fermi-surface geometry. This relationship is defined by the equations of motion for an electron in a magnetic field B:

$$\hbar\frac{d\vec{k}}{dt} = e(\vec{v}\times\vec{B}), \quad \vec{v}=\hbar^{-1}\nabla_k E \ ,$$

where $\vec{k}$ is the wave vector, $\vec{v}$ is the velocity, and E is the energy of the electron. These equations show that k_B, the component of $\vec{k}$ parallel to the field, is constant, as is the energy E. In this paper, the path of an electron in $\vec{k}$ space will be called an orbit to distinguish it from a trajectory, its path in real space. Every orbit is the intersection of the plane $k_B = \text{const}$ with the surface $E = \text{const}$. The electrons that are observed are those that can make transitions to unfilled states upon interaction with the rf field. These electrons must lie within kT of the Fermi energy, since a typical interaction changes the energy by only 10^{-7} eV. Therefore, the orbits that are observed will be intersections of a plane $k_B = \text{const}$ with the Fermi surface $E = E_F$.

The equations of motion also relate the components of $\vec{k}$ with the components of $\vec{r}$, the real-space position of the electron. Integration over time shows that the $\vec{k}$-space orbit is geometrically similar to the projection of the real-space trajectory onto a plane normal to $\vec{B}$. The orbit is rotated by $\frac{1}{2}\pi$ relative to the trajectory and their dimensions are related by $k=(eB/\hbar)r$.

A typical orbit and its corresponding trajectory are shown in Figs. 2(a) and 2(b), respectively. The upper drawings are views along the magnetic field and show the similarity of the motions and the relative rotation by $\frac{1}{2}\pi$. The lower views demonstrate that while the orbit must be planar, the trajectory need not be. In this example, the trajectory is not even closed, since it has a net average velocity parallel to $\vec{B}$. But the similarity of the orbit and the trajectory in the plane normal to $\vec{B}$ means that a caliper measurement on the trajectory in this plane can be converted to a corresponding caliper dimension on the Fermi surface: $k_c = eB_c d/\hbar$, where B_c is the magnetic field value for which the trajectory has a caliper dimension equal to the sample thickness d. Since the caliper on the trajectory is measured along the direction $\vec{n}$ (the normal to the sample surface), the Fermi-surface caliper k_c is measured along the direction $\vec{n}\times\vec{B}$.

Not all orbits on the Fermi surface can be measured by the RFSE. The experimental detection of any particular interaction between the rf field and the electrons in the sample requires that a substantial number of electrons be taking part. These electrons must be following trajectories which have nearly identical caliper dimensions. This implies that the corresponding $\vec{k}$-space orbits must also have nearly identical caliper dimensions. Since the orbits are distinguished by their value of k_B, this condition means that the caliper k_c is stationary with respect to k_B, $dk_c/dk_B = 0$. This stationary condition is the dominant factor determining which Fermi-surface calipers are seen in the experiment. Such selectivity is particularly important for simplifying the interpretation of the experimental data.

It should be noted that not all of the excited electrons have necessarily received the excitation at the surface of the sample. Many of the internal field spikes are strong enough to act as secondary skin layers for excitation of other electrons. This effect gives rise to the phenomenon of "chains" of coupled trajectories, where each link (except the first) is excited by interaction with the field spike caused by the previous link. This is depicted in Fig. 3. Such a trajectory chain appears in the data much like any other trajectory, except that its dimension does not correspond to a Fermi-surface dimension. This causes some complication in the interpretation of the data, particularly if one or more of the links is not ob-

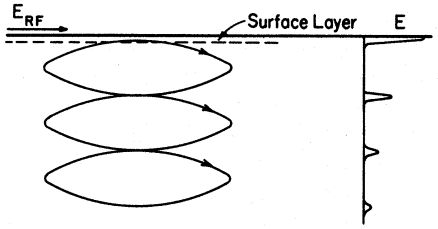

FIG. 3. Cross section of sample showing coupled trajectories.

served independently. Figure 3 represents a case that was actually observed in the experiment, where one, two, and three identical coupled trajectories were observed at fields of B_0, $2B_0$, and $3B_0$, respectively. The corresponding dimension on the Fermi surface is then

$$k_c = \frac{eB_0 d}{\hbar} = \frac{1}{2}\frac{e(2B_0)d}{\hbar} = \frac{1}{3}\frac{e(3B_0)d}{\hbar} \quad .$$

III. EXPERIMENT

The geometry of the experiment is shown in Fig. 4. A thin flat monocrystalline plate of magnesium is placed in a rf coil. A static magnetic field is also present, oriented parallel to the surface of the sample. The coil and sample are immersed in liquid helium at a temperature ranging from 1.2—4.2 °K.

The coil is part of the tank circuit of an rf oscillator, of frequency about 800 kHz. The level of oscillation in the coil is a sensitive function of the total power absorbed in the tank circuit. Therefore, any power absorption in the metal sample will be seen as a change in this level of oscillation, which is amplified and detected. Figure 5 is a block diagram of the electronics. Since the static magnetic field is modulated at 50 Hz, any field-dependent power absorption in the sample will cause amplitude modulation of the rf at this frequency. This modulation is detected at the detector stage and amplified in the audio amplifier before being fed to the lock-in amplifier. The limiter serves to remove the modulation from

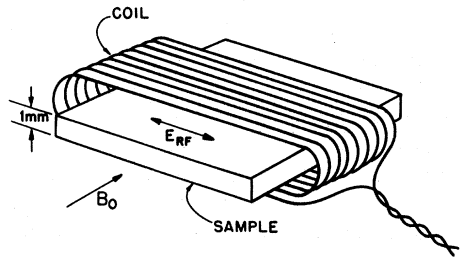

FIG. 4. Experimental geometry showing sample and rf coil.

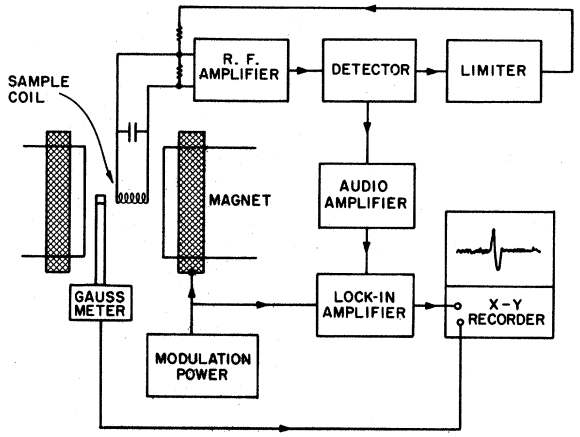

FIG. 5. Block diagram of experimental apparatus.

the rf signal before feeding it back to the tank circuit to complete the oscillator loop.

As already described, this experiment depends on the interaction of the electron motion with the physical boundaries of the sample. In order that the entire sample be effective, it is essential that it have a unique thickness. This requires that the faces be very flat and parallel and also free of any strains or damage.

The primary restriction on the sample thickness is that it must be less than the electron mean free path. This condition assures that the sample surfaces will have a dominant role in the scattering process. The very pure magnesium crystal used in this experiment has an electron mean free path of several millimeters at low temperatures. This simplifies the sample preparation, since a relatively thick sample (1.0 mm) could be used. Such a sample was much easier to handle and to machine to the required accuracy.

The technique employed in the sample preparation was electric-discharge machining (EDM). An irregular single crystal of magnesium was oriented to an accuracy of about 0.1° by x-ray diffraction. This orientation was carefully maintained while a slice was cut from the chunk using EDM with a fine traveling wire electrode (Cu wire, 0.003 in. diam). At this stage, the sample was approximately the correct thickness but was not sufficiently flat or parallel-sided. This was determined by observing the experimental signals from the sample at this stage of preparation. The signals were quite weak and broad but they improved substantially after the completion of subsequent stages of preparation. The position of the signals at the various stages was constant, after allowing for the slight changes in sample thickness.

The next step, spark planing, generated very

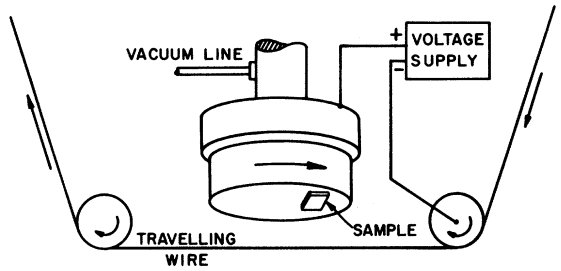

FIG. 6. Configuration for spark-planing of sample.

flat parallel surfaces. Figure 6 shows the configuration that was used, with the sample held by vacuum in a rotating head. This head was then lowered into contact with the fine traveling wire which had been aligned perpendicular to the axis of rotation. The rotation of the sample across the wire slowly spark-eroded all irregularities and generated a smooth plane surface. After one surface was planed, the sample was turned over and the procedure was repeated. Since the sample mounting surface was a plane normal to the axis of rotation (generated by an identical spark-planing procedure), the two surfaces of the sample were accurately parallel. Low spark currents were used at this step, so surface damage was minimized, leaving a surface roughness of about 10 μm. A light chemical etch in dilute HCl then removed most residual surface damage and gave a sample with a final thickness (at 0 °K) of 1.015 ± 0.005 mm.

The finished sample was then fastened in the center of the small rf coil and placed in the helium cryostat. The static magnetic field was adjusted so that it could rotate about the sample normal while keeping the field direction accurately parallel to the sample surface. The orientation of the field in the plane of rotation was measured to an accuracy of 0.1° and the magnitude of the field was determined to an accuracy of about 0.02 G by the use of standard NMR techniques.

Preliminary studies showed that the polarization of the rf field had a negligible effect. Therefore, no systematic variation of the polarization was made during the study of most of the experimental signals.

IV. DATA

The measurements on magnesium were made on a flat sample oriented normal to the $[11\bar{2}0]$ crystallographic axis. The static magnetic field was always parallel to the sample surface and data was taken over the full range of field orientation from [0001] to $[10\bar{1}0]$. For each orientation, the field strength was varied from below 0 to about 180 G. In the discussion that follows, the angle θ is the angle between the magnetic field direction and the [0001] axis.

Modulation of the static magnetic field by a small-amplitude field at 50 Hz permitted convenient phase-sensitive detection of signals. This modulation technique also meant that the observed signals were proportional to the first derivative of the power absorption with respect to the field. A typical data trace is shown in Fig. 7, taken for one particular field orientation $\theta = 40.7°$. This trace shows six distinct signals, of which several are clearly the result of trajectory coupling. The signal $\lambda + \lambda$ is observed to occur at twice the magnetic field at which the dominant signal λ occurs. The $\lambda + \lambda$ signal is clearly the result of two λ trajectories coupling together to span the sample thickness. This then accounts for the much smaller amplitude of the $\lambda + \lambda$ signal, since such a signal depends on coupling to a weak image field in the center of the metal sample. The signal labeled $\lambda + \mu_5$ similarly can be identified as arising from coupling, since it occurs at a magnetic field that is the sum of the magnetic fields for the signals λ and μ_5.

On the other hand, the signal $\lambda + \tau_2$ is also associated with coupled trajectories, but this is not obvious from the data. In this case, one of the fundamental signals (τ_2) has not been observed in the experiment. Therefore, there is no simple way to see the coupled nature of the signal $\lambda + \tau_2$, and misinterpretation is easy. The true identification will depend on an analysis to be presented in a later section.

The widths of the lines shown in Fig. 7 give a measure of the skin depth in the sample. If the width ΔB is measured between successive minima of the signal labeled λ, the fractional width $\Delta B/B_c$ is quite constant over a wide range of field and is equal to 0.030. According to line-shape calculations by Kaner and Gantmakher[9] $\Delta B/B_c \approx 6\delta/d$.

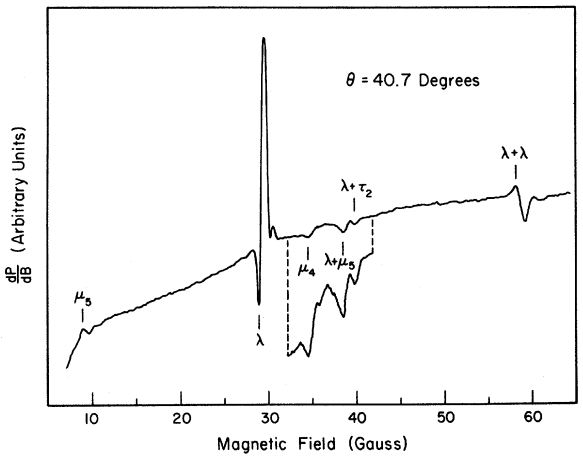

FIG. 7. Typical data trace.

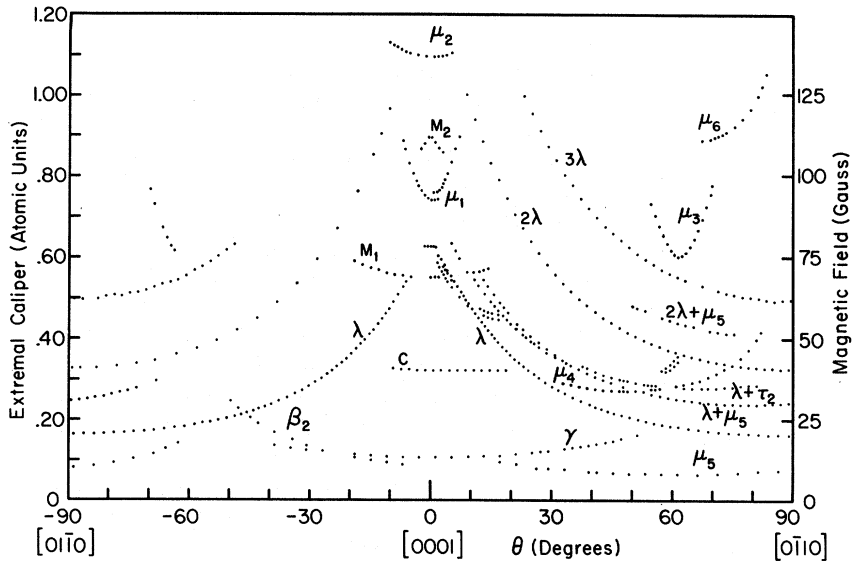

FIG. 8. Summary of observed experimental signals.

Since the sample thickness $d = 1.0$ mm, this implies $\delta \approx 5\times10^{-3}$ mm. This is in reasonable agreement with calculations of the anomalous skin effect at the experimental frequency (800 kHz).

The inset in Fig. 7 shows the increased sensitivity that can be achieved by the use of longer integration times and higher amplification. One can also see the problem caused by the slope of the baseline. In the lower field region, around 0—10 G, this slope is so large that it is difficult to use enough gain to see some of the small signals. This problem was overcome by detecting the signals at 100 Hz, the second harmonic of the modulation frequency. This technique discriminated against the smoothly varying background and permitted sensitive detection of the signals of interest (which were then proportional to the second derivative of the power with respect to the field).

In order to use one of these signals for an accurate determination of a Fermi-surface dimension, it is necessary to determine which part of the signal is important. Only one point on a signal corresponds to the exact fitting of the trajectory into the sample thickness. This is assumed to be near the low-field extremum, while the other structure in the signal is associated with the interaction of the trajectory with the fields in one or both skin layers. Previous experiments[10,11] show that the low-field extremum is least sensitive to changes in the skin depth and a recent computer study of the line shape by Juras[12] tends to confirm this interpretation. It can be concluded that some point on the low-field part of the line is the important point, but there is no conclusive evidence to indicate that it is the extremum. This point is generally chosen as a matter of convenience.

In addition, the observed line shapes vary widely and it is impossible to choose consistently equivalent points on every line. This is particularly true for weak signals where the line shape is difficult to compare with a reference. Such uncertainty is the major source of error in the calculation of Fermi-surface dimensions from RFSE data.

Figure 8 shows a summary of the experimental data, with each signal plotted as a point at the orientation and magnitude of the magnetic field at which it was observed. The magnetic field values are shown on the right and corresponding Fermi-surface calipers on the left. Dimensions in $\vec{k}$ space are in atomic units, 1 a.u. $= 1.89$ Å^{-1}.

A number of significant relationships can be seen in this data. Several of the curves lie nearly parallel to the curve λ. These are associated with chains of coupled trajectories which include the λ trajectory. It is important to recognize such couplings in order to avoid interpreting these signals as simple caliper dimensions.

The symmetries are also important in interpreting this data. The curve μ_3, for example, is symmetrical about $\theta = 62°$, which is the [0$\bar{1}$11] direction. The only caliper showing a minimum in this direction is associated with the second-zone surface; subsequent calculations will confirm this identification. Such symmetry information is most helpful in determining the particular piece of the Fermi surface with which a signal is associated.

An interesting and unexplained anomaly is seen in this data around $\theta = 0$, $B = 92$—95 G (signal labeled μ_1). In following this signal as the field is rotated, the data becomes double valued. This was only observed for the signal μ_1, for which some of the data traces are shown in Fig. 9. On either

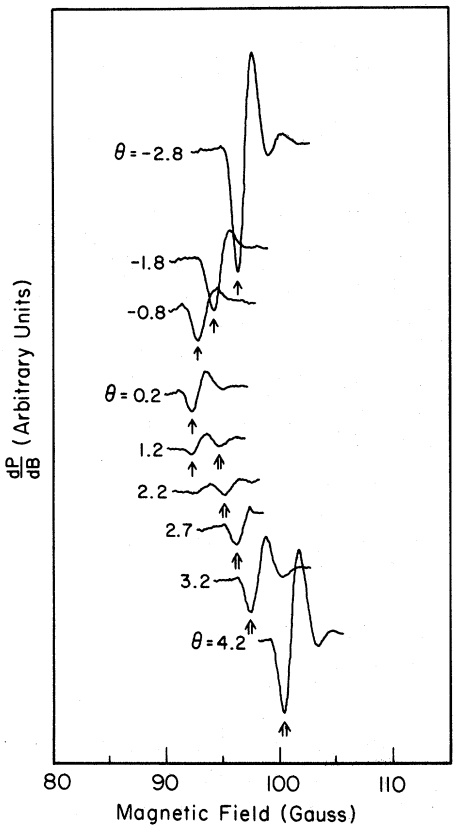

FIG. 9. Selected data traces for signal μ_1.

side of the symmetry plane ($\theta = 0$), similar signals are observed and one can readily locate the low-field minima that are assumed to be important. These are marked with a single arrow for $\theta < 0$, and a double arrow for $\theta > 0$. One would expect these points to become identical at $\theta = 0$. In fact, however, the points can be followed until they die out but they never coincide. Over a small range of angles ($\theta = 0.6° - 1.4°$) they coexist and this gives rise to the double-valued part of the data in Fig. 8. The signal amplitudes are not expected to be completely symmetrical about the planes of crystal symmetry, since the rf field is oriented arbitrarily with respect to the crystal axes. However, this would not explain such double-valued data.

All of the data shown in Fig. 8 is of little value unless the various calipers can be associated with particular parts of the Fermi surface. This problem of interpretation and identification is simplified by the fact that the Fermi surface of magnesium is quite close to the free-electron model. This permits the immediate identification of some of the data. For example, the calipers labeled λ have been replotted in polar coordinates in Fig. 10, along with the cross section (in the free-electron model) of the third-zone piece known as the lens. There can be little doubt about the identification of this data. Similar identifications can be made for other parts of the data, but such rough comparisons are inadequate for many of the signals, particularly those of complex origin. The interpretation of all the signals in terms of over-all caliper dimensions will give many dimensions that do not seem to fit the Fermi surface. But when more complicated effects are considered, such as partial trajectories or saddle-point influences, the proper interpretations can be made. In such cases as these, it is most important to have an accurate model of the Fermi surface to guide the interpretation. And having a convenient procedure for calculating orbit dimensions on this model greatly simplifies the comparisons.

V. FERMI-SURFACE MODEL

The mathematical model which has been used for detailed Fermi-surface calculations is based on the work of Kimball, Stark, and Mueller.[8] They have used very accurate de Haas—van Alphen data for Mg to determine the effective lattice potential to be used with a nonlocal pseudopotential calculation of the band structure. This model gives an accurate detailed representation of the entire

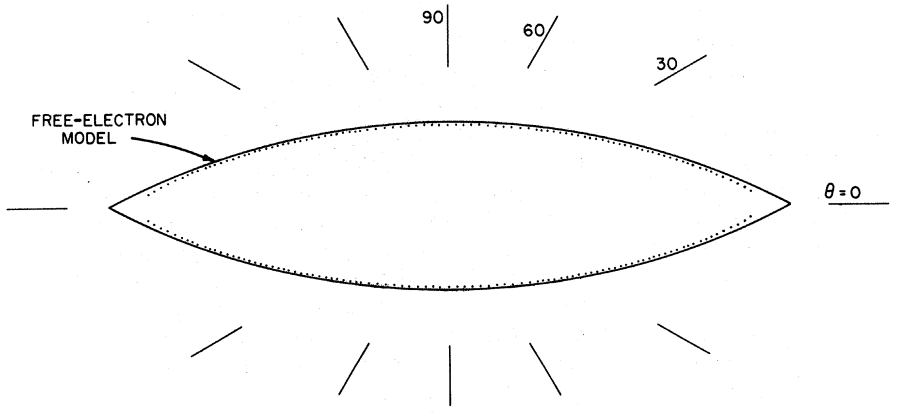

FIG. 10. Cross section of third-zone lens surface (free-electron model) compared to λ experimental calipers.

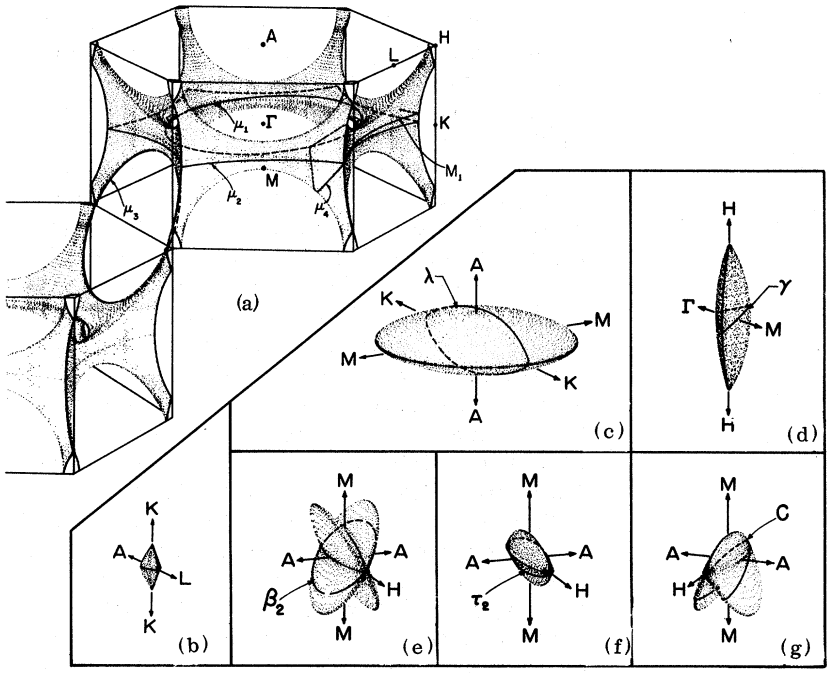

FIG. 11. Projection of calculated Fermi-surface points: (a) monster (second-zone holes); (b) cap (first-zone holes); (c) lens (third-zone electrons); (d) cigar (third-zone electrons); (e) butterfly (third-zone electrons); (f) fourth-zone electrons; (g) clam (combined third- and fourth-zone electrons).

Fermi surface and fits all of the known data for magnesium. However, this model is not convenient to use when extensive calculations are to be made. This band-structure model requires a matrix diagonalization for every calculation of $E(\vec{k})$. For calculating electron orbits on the Fermi surface $E(\vec{k})=E_F$, one wants $\vec{k}(E_F)$ and the velocity $\vec{v}(\vec{k})$ at a large number of points on each orbit. This requires inverting the function $E(\vec{k})$ numerically and calculating its gradient at each such point. This is prohibitively time consuming when one considers the many orbits that are required for the present analysis.

An alternative procedure has been adopted which greatly reduces the calculation time required and eliminates unnecessary duplication of orbit-point calculations. The first step is to use a computer to determine the exact location of the Fermi surface at a large number of closely spaced points. For each small region of the Fermi surface, an initial estimate is made of a value of $\vec{k}$ that lies on the surface $E(\vec{k})=E_F$. Then $E(\vec{k})$ is calculated (using the matrix diagonalization) and compared with E_F. If $E(\vec{k})\neq E_F$, the value of $\vec{k}$ is adjusted until $E(\vec{k})=E_F$. This final value is then on the Fermi surface and the gradient of $E(\vec{k})$ is calculated at this point to get the one-electron velocity $\vec{v}=\hbar^{-1}\nabla_k E(\vec{k})$. These values of $\vec{k}$ and $\vec{v}$ are stored on punched cards and the procedure is repeated in an adjacent small region of the Fermi surface.

The final result is an array of points that are accurately located on the Fermi surface. This array includes all of the pieces of the Fermi surface but extends only over $\frac{1}{24}$ of the Brillouin zone for each piece. The basic sector of the Brillouin zone is related by symmetry operations to the remainder of the zone. Therefore, the nearly 4000 points that have been calculated within this sector are equivalent to almost 100 000 points extending over the entire Fermi surface. The spacing of points is close enough that simple interpolation between points of this array is adequate to define the location of the Fermi surface to an accuracy of about 0.001 a.u. (For comparison, the height of the Brillouin zone is 0.6424 a.u.)

The result is shown in Fig. 11, which shows the computer-plotted projections of the points on each of the Fermi-surface pieces. These arrays of points form the basis for subsequent calculations of electron orbits on the Fermi surface. Typical orbits are also shown in Fig. 11, superimposed on the surfaces.

The first step in calculating an electron orbit is the determination of the plane in which it lies. The normal to the plane must be parallel to the magnetic field and the location of the plane is chosen to intersect the Fermi surface in the region of interest. Then the exact intersection of the plane with the Fermi surface is determined stepwise using the equations of motion. The array points already calculated are used with a simple interpolation procedure to define the position of the Fermi surface and the electron velocity at each step of the orbit. The result is an accurate determination of the wave vector $\vec{k}$ and the velocity $\vec{v}$ for the electron at a large number of points on

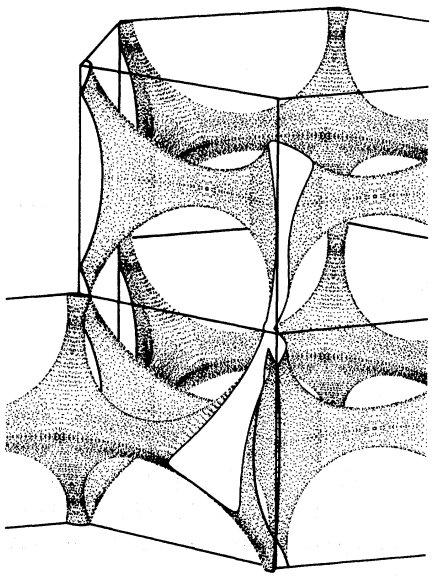

FIG. 12. Projection of monster in repeated zones showing location of orbit μ_6.

this orbit. In this way, the orbit dimensions, area, cyclotron mass, and corresponding real-space trajectory can be quickly calculated for any orbit.

As an indirect check on the accuracy of the model model and the method of calculation, each piece of the Fermi surface was sliced into a large number of parallel sections. That is, a series of closely spaced parallel orbits were calculated for each piece. The areas were calculated for all of the cross sections and then were integrated to find the volume enclosed by each piece of the Fermi surface. Since the surfaces in zones 1 and 2 are hole surfaces (energy increases toward the inside of the surface), the volume of these pieces should equal the volumes of the pieces in zones 3 and 4, which are bounded by electron surfaces. In Table I volumes are given in atomic units. The difference is less than 0.5% of the hole or electron volume, indicating that there is little possibility of any substantial error in either the basic mathematical model or the method used to calculate orbits.

VI. ORBIT CALCULATIONS

Figure 11 shows a few orbits that are typical of the many that were calculated using the procedure described above. The labels indicate the parts of the data (Fig. 8) to which the orbits correspond. (The justification of these identifications will be presented in a later section.) It is clear that the most complicated orbits will arise on the second-zone surface, the monster. This is because of its many saddle regions and because it is an open surface, i. e., it is connected across adjacent zones in the repeated-zone scheme. The orbits on this surface are, therefore, the most complicated to construct but are also the most interesting.

The procedure that was used on the monster, as well as on the other pieces, was to determine all possible electron orbits for the full range of magnetic field orientations. For a particular orientation of $\vec{B}$, calculations were made for all the orbits lying in a closely spaced set of planes normal to $\vec{B}$. These planes were placed throughout the Brillouin zone, with closest spacing in regions of particular interest. When the full set of possible orbits had been calculated for one orientation of $\vec{B}$, it was repeated for another orientation. The result is the accurate determination of essentially all the electron orbits, from the simplest to the most complicated.

In Fig. 12, an example of one of the more complex orbits calculated is shown. The figure is a projection of the monster in the repeated-zone scheme, truncated at the plane of the orbit. This orbit (which is associated with experimental signal μ_6) extends into three adjacent Brillouin zones, and exists only over a narrow band of the surface. Without the detailed computer calculations, its dimensions and even its existence would be uncertain.

The primary dimensions of interest on the calculated orbits are the caliper dimensions between turning points. Additional features that can be significant are saddle points and kinks in the orbit. All of these features are associated with current and field spikes in the sample if enough electron orbits have the same dimension and contribute simultaneously. To check this, it is necessary to look for dimensions that are stationary (usually extremal) with respect to variation of k_B. Only then will enough electrons be involved to give an observable signal.

For each such orbit dimension k_c that is found, one can expect to see an experimental signal. This will occur at the value of magnetic field which causes the corresponding trajectory dimension to just span the sample thickness: $B_c = \hbar k_c / ed$.

TABLE I. Volumes (in a.u.) of pieces in zones 1, 2, 3, and 4.

Zone 1	Volume = 0.000 319	
Zone 2	0.060 024	
Total for hole surfaces		0.060 343
Zone 3, lens	0.028 596	
cigar	0.003 091	
butterfly	0.024 588	
Zone 4	0.004 354	
Total for electron surfaces		0.060 629
Difference	0.000 286	

Therefore, a comparison of the calculated values of k_c and the experimental values of $edB_c/\hbar$ should serve to identify the data signals.

VII. SIGNAL INTERPRETATIONS

The interpretation and identification of the experimental signals depends on the model calculations in varying degrees. For the simplest signals, the nearly free-electron (NFE) model will suffice. But for much of the experimental data, more accurate and detailed calculations are essential. The following comparisons of the calculations with the experimental data will demonstrate this clearly.

The signals arising from the lens are the strongest and easiest to interpret. Figure 10 has shown the comparison of the experimental calipers with the free-electron model for this surface. Figure 13 shows the comparison of the same data with the accurate band-structure model. (The calculated values are represented by the solid curves.) The fit is seen to be excellent for both the fundamental signal and the spatial harmonics (coupled trajectories, see Fig. 3). However, this fit is the result of a small adjustment of one parameter. It has already been mentioned that the conversion of the experimental data to a Fermi-surface caliper depends on the choice of the appropriate point on the experimental signal. This choice is usually the low-field extremum, but for the present experiment this was not assumed. The data for the lens is sufficiently extensive and accurate to permit the independent determination of this point.

Using the RFSE measurements of the lens dimensions, one can calculate the area of the central cross section. This area determination will include the same uncertainty as the caliper dimensions. But the area can be directly compared to accurate de Haas—van Alphen data on Mg.[7] If the RFSE data is based on the low-field extremum, the area of the lens section is 3% larger than that determined by the de Haas—van Alphen effect. In terms of the relative accuracies of the RFSE data and the de Haas—van Alphen area, this deviation is significant.

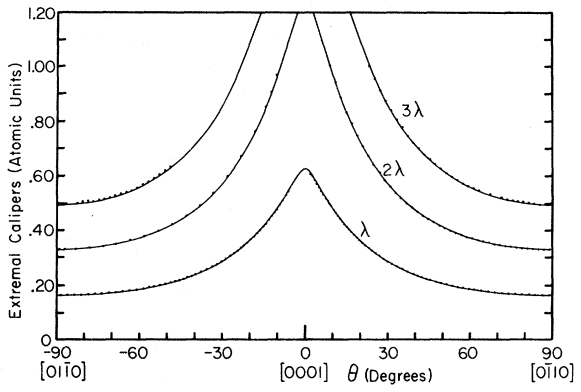

FIG. 13. Comparison of calculations and data for λ signal.

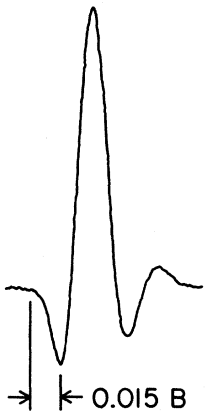

FIG. 14. Typical λ signal showing shift of the reference point.

To bring the areas into agreement requires a shift in the RFSE data of $(1.03)^{1/2}=1.015$. This can be done by shifting the relevant point on the experimental signal by 1.5% toward lower field. The effect on a typical λ signal is shown in Fig. 14. The relevant point on the signal is seen to shift from the extremum to the point where the signal first deviates from the base line. This seems to be a more logical point, since the position of the extremum depends on the signal processing.

Other studies have also concluded that the left edge of the signal is the correct point to choose. Koch and Wagner[4] base their observation on the known dimensions of the Fermi surface they studied (potassium), which is equivalent to the approach discussed above for the lens surface in Mg. Gantmakher and Krylov,[13] on the other hand, use the frequency dependence of the line shift. They show that only the left edge of the signal is independent of the frequency and therefore must correspond to the equality of the trajectory dimension to the sample thickness.

However, the left edge of the signal is difficult to locate precisely and consistently. For this reason, measurements on the signals were referred to the extremum in order to achieve relative accuracy in the positions. But all of the corresponding Fermi-surface calipers were diminished by a constant factor of 1.015 to make the results equivalent to choosing the left edge of the signal. This correction is included in all of the data in this paper, but should not be assumed to hold in the general case. It is presumably influenced by numerous geometrical and experimental factors.

The simple interpretation of the signals in terms of extremal caliper dimensions is adequate for the identification of the signals labeled γ, β_2, and C. These signals arise from orbits on the cigar,

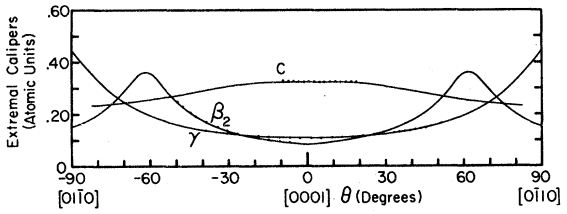

FIG. 15. Comparison of calculations and data for γ, β_2, and C signals.

butterfly, and clam, respectively [see Figs. 11(d), 11(e), and 11(g)]. The model calculations are not essential in making these identifications but they do clearly confirm the validity of these assignments. Although experimental factors prevented the observation of data corresponding to the full range of the calculations, the agreement is excellent for the data that is present, as shown in Fig. 15. The orbit C is of particular interest, since the clam surface exists only by virtue of magnetic breakdown between the butterfly and the fourth-zone surface.[14] This is the result of the very small energy gap between these two surfaces in the *AHL* plane and it has the effect of combining these two surfaces and producing a characteristic set of extremal caliper dimensions.

The remaining signals that can be interpreted in terms of simple caliper dimensions are associated with orbits on the monster. These are the signals μ_1, μ_2, μ_3, μ_4, and μ_6 shown in Figs. 11(a) and 12. The first three are relatively easy to identify from their symmetry and the angular dependence of their caliper dimensions. The signal μ_4 has less symmetry but was readily identified with the oblique orbit that encircles the junction of the "arms" of the monster.

The signal μ_6, on the other hand, probably would not have been correctly identified without the help of the model calculation. The position of this signal indicated a caliper dimension that is larger than the Brillouin zone and forces one to consider orbits that extend into adjacent zones. Such orbits tend to be quite complicated and the model calculation is essential in searching for extremal caliper dimensions. Figure 12 shows the orbit that was finally identified with μ_6.

Figure 16 presents the comparison between the experimental data and the model calculations for these orbits. Again the agreement is very good and confirms the accuracy of both the experimental data and the Fermi-surface model.

Of the signals that remain, several are obviously caused by trajectory coupling. This applies to the signals labeled $\lambda+\mu_5$ and $2\lambda+\mu_5$ in Fig. 8, as well as to the spatial harmonics of the λ signal. It is not surprising that all of the observed couplings include the λ trajectory. This happens for the same reason that the λ trajectory dominates the experimental signals: This trajectory is very efficient in coupling electronic motion to the rf field. No other trajectory can couple efficiently enough to the weak internal fields to produce an observable coupled signal.

Since the signals associated with coupled trajectories do not provide new caliper information, it is useful to eliminate them at the beginning. This can usually be done by recognizing their additive relationship to the fundamental signals. But for one signal, labeled $\lambda+\tau_2$ in Fig. 8, this was not possible. Although this signal seemed likely to arise from coupling to the λ trajectory, no signal was observed for the other trajectory alone. This made it difficult to conclude that the signal arose from coupling. The alternative was to interpret this signal as a simple caliper, but no fit could be found to this caliper dimension. Approximate fits or distortions of the Fermi surface could not be permitted in view of the very good fits that had been made to most of the other data.

But the model calculation shows that the τ_2 orbit on the fourth-zone surface [see Fig. 11(f)] is just the right size to give this signal when the corresponding trajectory is coupled to the λ trajectory. This caliper is plotted in Fig. 17 along with the calculated value of $\lambda+\tau_2$. This close fit is a convincing argument for this assignment but it does not explain the absence of the τ_2 signal in the experimental data. This absence of an expected signal is one of the major problems in the interpretation of RFSE data.

One of the most difficult identifications was for the data labeled μ_5 in Fig. 8. There is no particular symmetry to the data and it indicates a Fermi-surface caliper dimension that is too small to match any part of the surface. At this point, it becomes necessary to consider the possibility of a partial trajectory giving rise to this signal. Partial trajectories will necessarily give weaker signals be-

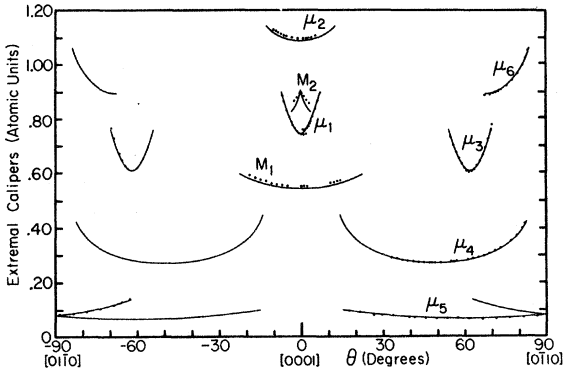

FIG. 16. Comparison of calculations and data for signals associated with the monster.

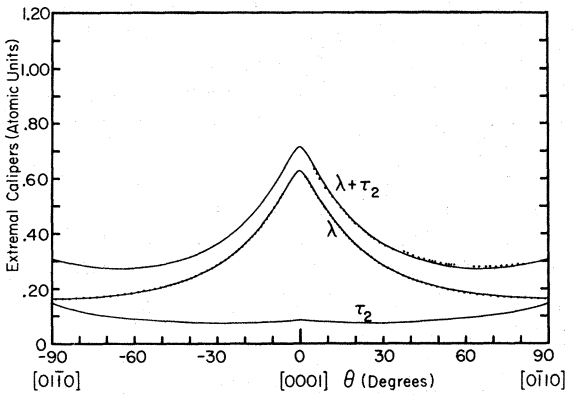

FIG. 17. Comparison of calculations and data for $\lambda+\tau_2$ signal.

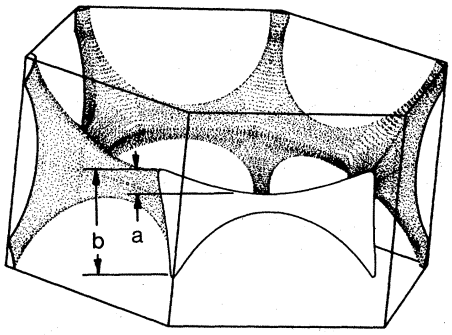

FIG. 18. Projection of monster showing location of orbit μ_5.

cause the electrons on such trajectories are scattered out of this effective state when they strike the sample surface. It is for this reason that partial trajectories have not been given primary consideration.

The entire set of calculated orbits were studied in an effort to find some orbit section (between turning points) that is the right size for this signal. The result is an orbit on the monster shown in Fig. 18. The caliper dimension b between outer turning points is not extremal and is not observed. But the smaller caliper dimension a *is* extremal and matches the experimental data over a wide range of field orientations.

Figure 19 shows the comparison of the calculations and the data for this signal as well as the signals previously identified as couplings of the μ_5 trajectory. The actual λ and μ_5 trajectories are drawn in Fig. 20. This shows the geometry of the coupling and a schematic plot of the electric field E in the sample.

The signal labeled M_1 (see Fig. 8) was observed over a substantial range of field orientation and indicated a caliper dimension fairly close to the dimensions of several pieces of the Fermi surface. But none of the fits was good enough to give confidence in the assignment. The possibility of a partial trajectory giving this signal was again considered, with the result that M_1 has now been identified with an orbit segment on the outside of the monster [see Fig. 11(a)]. But this segment is not between turning points. It is between one turning point and a break or kink in the orbit. Such a sharp discontinuity in the electron motion gives a corresponding discontinuity in the internal field and current and causes the observable signal.

The last signal to be identified is labeled M_2 in Fig. 8. The symmetry and position of this signal suggest an orbit on the monster. But again no direct fit was found that was good enough. In this case, no partial trajectory seemed to explain the signal either. It was finally realized that this signal must be connected with electrons moving in the saddle regions of the monster. In each saddle region, the radii of curvature in the principal planes are of opposite sign. The significant feature of such a region is that an electron orbit of finite size can come arbitrarily close to a point at which the electron velocity is parallel to the magnetic field. Such a point will be referred to as a saddle point. In the previous discussions, motion along the magnetic field was usually small and was ignored. But to understand the influence of a saddle point, it is important to consider the full three-dimensional motion of the electron.

If a $\vec{k}$-space orbit contains a saddle point, an electron moving along this orbit will stop when it reaches the saddle point. Here the driving force, which is proportional to $\vec{v}\times\vec{B}$, is zero. If the orbit only passes close to the saddle point, the driving force becomes small but not zero. Therefore, the electron will continue around the orbit, but will spend a long time in the vicinity of the saddle point. In real space, the corresponding motion is nearly parallel to the magnetic field. This is shown in

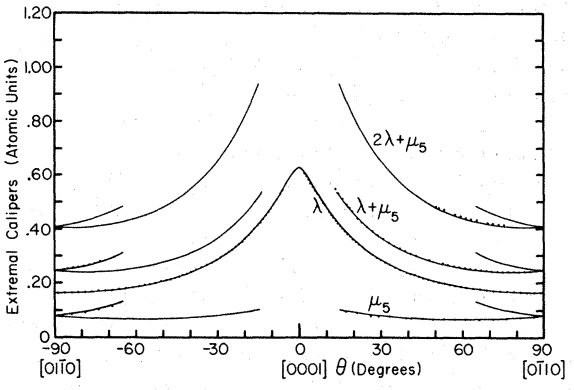

FIG. 19. Comparison of calculations and data for μ_5 signal.

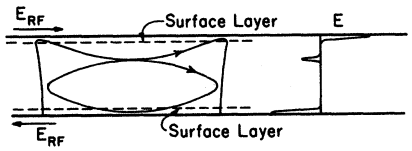

FIG. 20. Cross section of sample showing λ and μ_5 trajectories.

Fig. 21, where the trajectory associated with the signal M_2 has been plotted by the computer. [Another view of this trajectory was shown in Fig. 2(b).] The saddle-point motion is at the very top and bottom of the downward spiral. At these points the velocity is nearly parallel to $\vec{B}$, and therefore nearly parallel to the surface. These parts of the trajectory can be just as effective as the usual turning points in interacting with the external rf field. In Fig. 21(a), the positions of the sample surfaces for interaction with the outer turning points of this trajectory are drawn. But these turning points are quite sharp and are not very effective in interacting with the rf field. The inner turning point and the saddle-point motion are much more effective but can enter the skin layer only after trajectory cutoff. This condition is shown in Fig. 21(b), with the effective points indicated by small circles. In spite of the fact that trajectory cutoff prevents the electrons from making repeated returns to the skin layer, this trajectory segment is sufficiently effective to give an observable signal. The calculated caliper dimensions for this segment are compared to the M_2 experimental observations in Fig. 16. This figure summarizes the comparisons for all signals that are associated with the monster.

VIII. CONCLUSION

Virtually all of the data in Fig. 8 have been identified, i. e., correlated to specific Fermi-surface orbits and dimensions. Only after all the identifications are made is it apparent how many different effects can contribute to the observed signals. This is one of the major drawbacks in the use of RFSE in studying unknown Fermi surfaces. Since line shapes give no clear guide to the interpretation of the signals, it becomes very easy to misinterpret substantial parts of the experimental data.

In the case of the RFSE in magnesium, five prominent signals could not properly be interpreted in terms of simple caliper dimensions. The signal $\lambda + \tau_2$ was not readily recognized as being associated with coupled trajectories since the τ_2 signal was not observed. On the other hand, μ_5 was observed both alone and coupled. With this much experimental data depending on the identification of the μ_5 signal, it was certain that some sort of identification would be made. But without the model calculation as a guide, it is unlikely that the identification would have been correct. Very detailed calculations on an accurate model are required to discover the partial orbit segments that have an extremal caliper. Such calculations were also necessary for the identification of the M_1 signal. Such identifications would be virtually impossible for an unknown Fermi surface. This shows the problems in using the RFSE for exploring any but the simplest Fermi surfaces.

The signals C and M_2 required even more complex interpretations. The signal C is caused by magnetic break-down effects and M_2 is strongly affected by saddle-point motion. Such effects might not have been considered if the Fermi surface had been poorly known. The model calculation was essential to prevent misinterpretation of these signals.

Another example of the need for an accurate model is in the work on tin. Gantmakher's extensive work on tin[1] first clearly demonstrated the potential of the RFSE. But his original interpretations of the data were based on the NFE model. This permitted the correct identification of only a few signals and led to the misinterpretation of several. For example, signals 3_1, 5_1, and 3_2 [see Ref. 1(c)] were attributed to the surface in zone 4(b), while in fact they arise from orbits in zone 5. Only a small part of the data could be clearly identified using the NFE model.

Weisz[15] then used Gantmakher's RFSE data to guide the calculation of a local pseudopotential model of the Fermi surface of tin. This model was

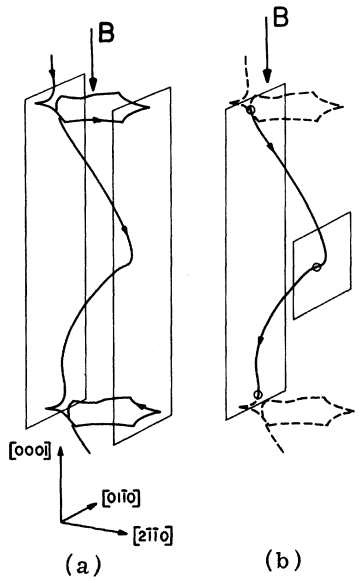

FIG. 21. Trajectory M_2 showing positions of sample surfaces for interaction (a) with outer turning points and (b) with the inner turning point and saddle-point motion.

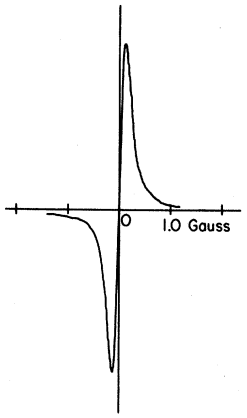

FIG. 22. Signal observed at zero magnetic field.

a big improvement over the NFE model and was used to explain most of Gantmakher's signals. However, the fit to the RFSE data was not very good. Subsequent de Haas—van Alphen area measurements[16] on the tin Fermi surface revealed further inaccuracies in Weisz's model.

Craven[17] used this de Haas—van Alphen data to calculate an improved Fermi-surface model. Although this model was constrained to fit the dHvA data, it was also found to give an excellent fit to virtually all of Gantmakher's RFSE data. This agreement justified and extended the previous interpretations of Gantmakher's data and also confirmed the high accuracy of the data itself.

This example further illustrates the weakness of the RFSE for determining the geometry of unknown Fermi surfaces. To take full advantage of the extensive and accurate data provided by the RFSE requires prior knowledge of the Fermi-surface geometry. But when this is the case, the variety of signals can be properly interpreted and used to study other aspects of the dynamics of the conduction electrons.

One example of this is the determination of the electron mean free path in the metal. By studying the dependence of the signal amplitude on the tip angle of the magnetic field,[18] one can determine the free mean path for particular groups of electrons on the Fermi surface. The study of the temperature dependence of the amplitudes[19] can give the temperature dependence of the mean free path. But such studies are possible only for particular types of signals, and this requires the identification of any signal that is to be used.

Another application of the RFSE is the use of the electron trajectories as probes for sampling the rf field distribution in the metal. Such an application can give valuable information about the surface conductivity in the presence of a magnetic field. At the same time, the full utilization of this technique will require a thorough understanding of the factors influencing the line shapes. This is an area where much work remains to be done.

ACKNOWLEDGMENTS

This work has been supported by the National Science Foundation and, to a lesser extent, by the Advanced Research Projects Agency through its support of the Materials Preparation Laboratory at the University of Chicago. Fellowship support during the course of the work was generously provided by the National Aeronautics and Space Administration and the Shell Oil Company. I would especially like to thank Professor R. W. Stark for his advice and encouragement.

APPENDIX

The experiment also yielded one signal that is apparently unrelated to the RFSE. This signal was observed at zero magnetic field and showed little dependence on the orientation of the field with respect to the crystalline axes. (The field was kept parallel to the sample surface, however.) The first derivative of the signal is shown in Fig. 22, where the peaks are at ± 0.12 G. Somewhat similar observations have been made by others.[20,21]

A possible explanation, suggested by Koch,[22] is that these signals arise from electrons in skipping trajectories at the surface of the sample. But for these quantized trajectories to be effective, the magnetic field must be large enough to confine them to the skin layer. The magnetic field required to confine the first n quantized trajectories to the skin depth δ is given by

$$B = (\hbar/2ek_F)[A(n)/\delta]^3,$$

where k_F is the wave vector of the electrons and $A(n)$ is given by $[1.5\pi(n-0.25)]^{2/3}$. For magnesium, a magnetic field of 0.12 G will confine the first 13 trajectories to a skin layer of thickness 2.0 μm. Although this explanation is only tentative, the calculations are consistent with the observations and make this explanation plausible.

---

†Presented as a thesis to the Department of Physics, The University of Chicago, in partial fulfillment of the requirements of the Ph.D. degree.

[1](a) V. F. Gantmakher, Zh. Eksperim. i Teor. Fiz. 42, 1416 (1962)[Sov. Phys. JETP 15, 982 (1962)]; (b) *ibid.* 43, 345 (1962) [*ibid.* 16, 247 (1963)]; (c) *ibid.* 44, 811 (1963) [*ibid.* 17, 549 (1963)]; (d) *ibid.* 46, 2028 (1964)[*ibid.* 19, 1366 (1964)].

[2]V. F. Gantmakher, in *Progress in Low Temperature Physics*, edited by C. J. Gorter (North-Holland, Amsterdam, 1966), Vol. 5, p. 181.

[3]W. M. Walsh, Jr., *Electrons in Metals* Vol. 1 of *Solid State Physics*, edited by J. F. Cochran and R. R. Haering (Gordon and Breach, New York, 1968), p. 127.

[4]J. F. Koch and T. K. Wagner, Phys. Rev. 151, 467 (1966).
[5]D. M. Sparlin and D. S. Schreiber, in *Proceedings of the Ninth International Conference on Low Temperature Physics, Columbus, Ohio*, 1964, edited by J. G. Daunt, D. O. Edwards, F. J. Milford, and M. Yaqub (Plenum, New York, 1965), p. 823.
[6]J. B. Ketterson and R. W. Stark, Phys. Rev. 156, 748 (1967).
[7]R. W. Stark, Phys. Rev. 162, 589 (1967).
[8]J. C. Kimball, R. W. Stark, and F. M. Mueller, Phys. Rev. 162, 600 (1967).
[9]E. A. Kaner and V. F. Gantmakher, Usp. Fiz. Nauk 94, 193 (1968) [Sov. Phys. Usp. 11, 81 (1968)].
[10]A. Fukumoto and M. W. P. Strandberg, Phys. Letters 23, 200 (1966).
[11]I. P. Krylov and V. F. Gantmakher, Zh. Eksperim. i Teor. Fiz. 51, 740 (1966) [Sov. Phys. JETP 24, 492 (1967)].
[12]G. E. Juras, Phys. Rev. 187, 784 (1969).
[13]V. F. Gantmakher and I. P. Krylov, in *Proceedings of the Tenth International Conference on Low Temperature Physics, Moscow, U.S.S.R.*, 1966 (VINITI, Moscow, 1967), Vol. 3, p. 128.
[14]See Ref. 6, p. 759; the first two figure references on this page should read Figs. 12(a) and 12(b).
[15]G. Weisz, Phys. Rev. 149, 504 (1969).
[16]J. E. Craven and R. W. Stark, Phys. Rev. 168, 849 (1968).
[17]J. E. Craven, Phys. Rev. 182, 693 (1969).
[18]V. F. Gantmakher and I. P. Krylov, Zh. Eksperim. i Teor. Fiz. 47, 2111 (1964) [Sov. Phys. JETP 20, 1418 (1965)].
[19]V. F. Gantmakher and Yu. V. Sharvin, Zh. Eksperim. i Teor. Fiz. 48, 1077 (1965) [Sov. Phys. JETP 21, 720 (1965)].
[20]V. F. Gantmakher and Yu. V. Sharvin, Zh. Eksperim. i Teor. Fiz. 39, 512 (1960) [Sov. Phys. JETP 12, 358 (1961)].
[21]J. F. Cochran and C. A. Shiffman, Phys. Rev. 140, A1678 (1965).
[22]J. F. Koch, *Electron in Metals*, Vol. 1 of *Solid State Physics*, edited by J. F. Cochran and R. R. Haering (Gordon and Breach, New York, 1968), p. 278.

PHYSICAL REVIEW B VOLUME 4, NUMBER 6 15 SEPTEMBER 1971

Transient Imperfections. The Propagation of Waves along a Line of Lattice Atoms†

J. S. Koehler
Department of Physics, University of Illinois, Urbana, Illinois 61801
(Received 26 April 1971)

Motion of atoms along a close-packed row of atoms in a crystal is described. Each atom has a sinusoidal interaction with atoms not in the row. It also interacts by Hooke's law with its nearest neighbors in the row. For wavelike solutions, the displacements of the nearest neighbors are expanded in terms of time derivatives of the displacement of the atom in question. If this expansion converges, then solutions are obtained in both the classical and the quantum cases. In the classical case, seven different types of solutions are found. In the classical case, the conditions such that the atoms move over the potential barrier are carefully investigated. Conditions are given under which two waves give motion over the barrier when neither would separately. Similar considerations are given for combinations of three waves. Convergence does occur for reasonable potentials.

I. INTRODUCTION

There is a very great need for investigations both by theory and experiment of lattice motions which are large and hence anharmonic. In this paper we discuss the propagation of lattice waves along a line of atoms in a crystal. The motion will not be limited to small amplitude; in fact, the conditions under which atoms can move over the potential barriers which limit them to vibration in a given valley will be carefully examined.

II. FRENKEL-KONTOROVA MODEL

Consider a monatomic crystal composed of mass points m between which there are forces of interaction. Let us focus our attention on a line of atoms lying along some prominent crystallographic direction. The motions which will be described are undoubtedly of most importance for directions having closely spaced atoms and having neighboring rows which are not too near the line. The $\langle 110 \rangle$ directions in the fcc lattice represent such a case. Let the potential for motion along the line, i.e., along x, be composed of two parts. First an interaction of the jth atom on the line with the atoms of the lattice not on the line. This we write

$$V_{je} = \tfrac{1}{2} V_0 [1 - \cos(2\pi x_j/a)] , \quad (1)$$

where V_0 is the amplitude of the off-axis potential, x_j is the displacement of the jth atom from equilibrium in a direction along the line and a is the period of this off-axis potential. There is also an in-